ANNUAL REVIEWS

Annual Review of Condensed Matter Physics

Studying Quantum Materials with Scanning SQUID Microscopy

Eylon Persky,[1] Ilya Sochnikov,[2,3] and Beena Kalisky[1]

[1]Department of Physics and Institute of Nanotechnology and Advanced Materials, Bar-Ilan University, Ramat Gan, Israel; email: beena@biu.ac.il

[2]Department of Physics, University of Connecticut, Storrs, Connecticut, USA

[3]Institute of Materials Science, University of Connecticut, Storrs, Connecticut, USA

Annu. Rev. Condens. Matter Phys. 2022. 13:385–405

First published as a Review in Advance on December 21, 2021

The *Annual Review of Condensed Matter Physics* is online at conmatphys.annualreviews.org

https://doi.org/10.1146/annurev-conmatphys-031620-104226

Keywords

quantum sensing, scanning probe microscopy, correlated electrons

Abstract

Electronic correlations give rise to fascinating macroscopic phenomena such as superconductivity, magnetism, and topological phases of matter. Although these phenomena manifest themselves macroscopically, fully understanding the underlying microscopic mechanisms often requires probing on multiple length scales. Spatial modulations on the mesoscopic scale are especially challenging to probe, owing to the limited range of suitable experimental techniques. Here, we review recent progress in scanning superconducting quantum interference device (SQUID) microscopy. We demonstrate how scanning SQUID combines unmatched magnetic field sensitivity and highly versatile designs, by surveying discoveries in unconventional superconductivity, exotic magnetism, topological states, and more. Finally, we discuss how SQUID microscopy can be further developed to answer the increasing demand for imaging new quantum materials.

INTRODUCTION

Novel quantum phenomena are often driven by cooperation, or competition, between different electronic properties with similar energies. For example, unconventional superconductors may emerge when magnetism and superconductivity, which are typically opposing ordering phenomena, team up. Experimentally studying coexisting orders poses several challenges. First, a single probe is typically well-suited to study only a single aspect of the system, necessitating multiple complementary studies to fully uncover the underlying orders. Second, when only a small portion of the electrons participate in a certain order, sensitive, noninvasive sensors are required. One approach to tackle these issues is mesoscale magnetic imaging. Magnetic fields are generated by both charge currents and localized moments. This enables studying magnetism, superconductivity, and normal current flow with a single sensor. Sensitive local probes can access small electronic populations or weak spatial modulations. Among the growing variety of magnetic probes (1–3), scanning superconducting quantum interference device (SQUID) microscopy (SSM) is the unbeatable choice when high field sensitivity and noninvasiveness are required. SSM can also be easily reconfigured to enable additional modalities such as local thermometry and susceptometry. Combined, sensitivity and versatility allow the probing of a broad range of electronic orders.

In this review, we survey some of the discoveries enabled by SSM in the past decade. We first discuss design considerations and the trade-off between field sensitivity and spatial resolution. We then review studies of a variety of fundamental electronic phenomena: superconductivity, magnetism, topological phases, and lattice effects. We conclude with an outlook on the next-generation SQUID sensors, and the new research endeavors they will enable.

SCANNING DC SQUID MICROSCOPY

A DC SQUID consists of a superconducting loop, interrupted by two Josephson junctions (JJs; 4, 5). When the current flowing in the loop exceeds the junctions' critical current, a voltage develops across the loop. To maintain fluxoid quantization in the SQUID loop in the presence of external magnetic flux, the superconductor generates a screening current periodic in the external flux. As a result, the critical current and the voltage drop across the device are periodic in the external magnetic flux, with a period of the flux quantum, $\Phi_0 = h/2e$, where h is Planck's constant and e is the electron charge.

For SQUID microscopy, a successful design balances two characteristics: spatial resolution and magnetic field sensitivity. The spatial resolution is determined by the sensor-sample distance and the size of the magnetic pickup area. A small pickup area can be achieved in several ways. One is to fabricate a small SQUID loop (6–10; **Figure 1*a–c***); a sample can then be placed near or fabricated on the nano-SQUID, or the SQUID can be scanned over a sample. In a SQUID on a tip configuration (**Figure 1*a***), a SQUID loop is fabricated on the apex of a pipette, which is scanned over the sample surface (11). A second approach is to fabricate a larger SQUID loop and extend a small pickup coil away from the junction (12–14; **Figure 1*d***). The pickup loop of these chip-based planar SQUIDs is then scanned over the sample to produce magnetic field images. Fabrication procedures have been improved over the years, and scanning SQUIDs are now available with loops from 10 mm (15, 16) to 40 nm (17) in diameter. Note that for small loops, the effective pickup area is larger than the loop's inner diameter owing to magnetic field line distortions from the finite loop thickness (18).

The magnetic field resolution is determined by the SQUID's rms magnetic flux noise, $S_\Phi^{1/2}$, and by the effective pickup area, $S_B^{1/2} \approx S_\Phi^{1/2}/A_{\text{eff}}$. Although SQUIDs can be fabricated using a diverse array of techniques, their flux sensitivity is determined by the current noise at the

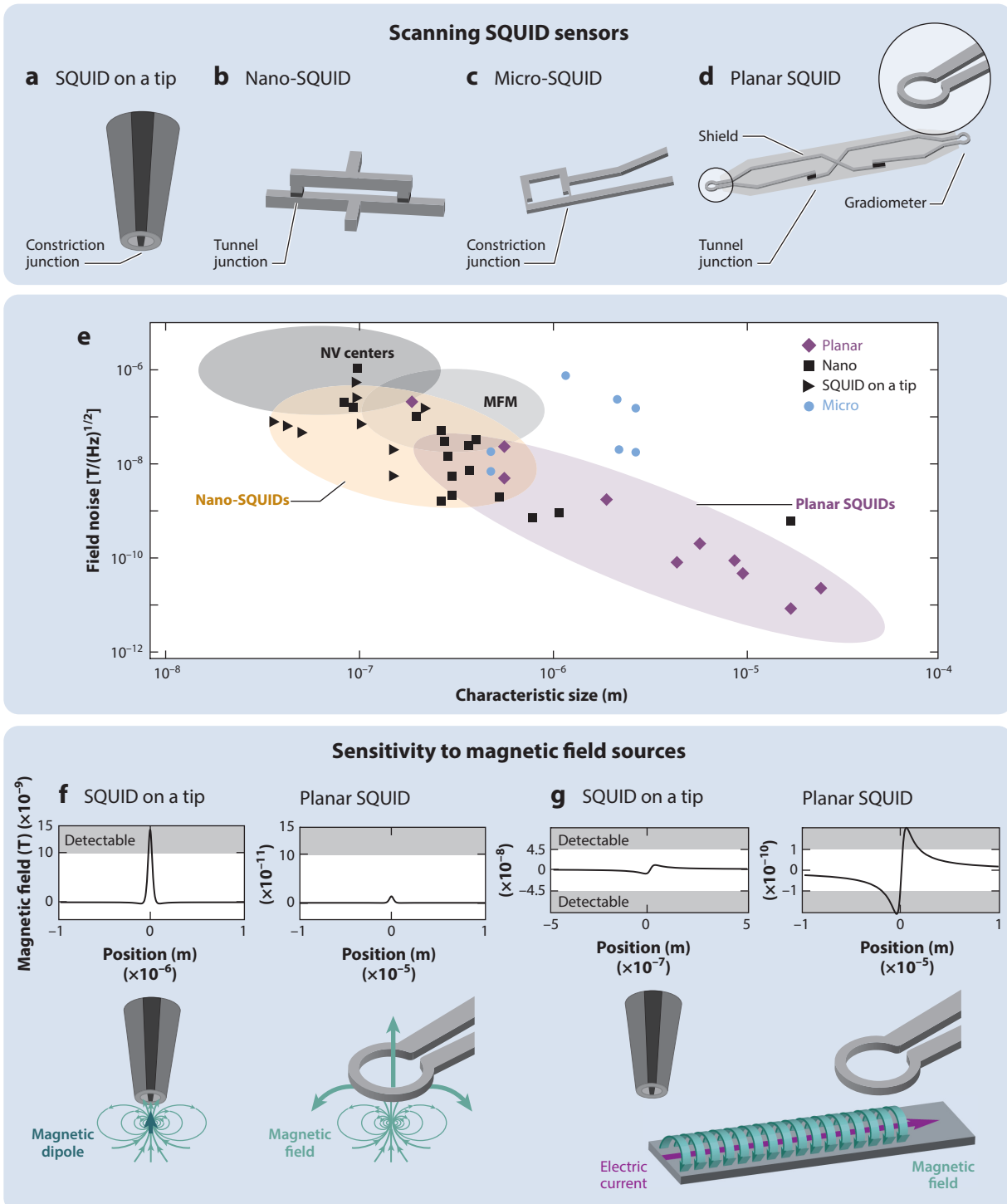

(Caption appears on following page)

Figure 1 (*Figure appears on preceding page*)

Scanning SQUID microscopy. (*a–d*) Representative sensor geometries, showing various ways to fabricate SQUIDs with a small sensing (pickup) area. (*e*) Magnetic field noise versus spatial resolution for various SQUIDs. Different sensor geometries occupy complementary regions in the graph; at the expense of spatial resolution, the field sensitivity of SQUID magnetometers can be improved by orders of magnitude. The performance of other magnetic imaging techniques—MFM and diamond NV center magnetometry—is estimated from References 19–22. (*f*,*g*) Sensitivity to different magnetic field sources. (*f*) Magnetic fields above a 1-μ_B point dipole at heights of 100 nm (*left*) and 1 μm (*right*). The shaded gray areas indicate the detectable fields for a SQUID on a tip (*left*) and for a planar SQUID (*right*). (*g*) Same as in panel *f* but for a one-dimensional wire carrying 1 nA. The optimal magnetometer choice is different for each source, owing to the different field profiles. Abbreviations: MFM, magnetic force microscopy; NV, nitrogen-vacancy; SQUID, superconducting quantum interference device.

junctions, S_I. In the low frequency regime there are two white-noise contributions to S_I: thermal fluctuations and shot noise (23–26). Although S_I can be expressed analytically, converting to S_Φ requires solving the Josephson equations, a task that can generally only be achieved numerically. A finite junction capacitance C, such that $\beta_C = 2\pi I_0 R^2 C/\Phi_0 < 1$, where I_0 and R are the junction's critical current and resistance, respectively, ensures that the *I–V* characteristics are not hysteretic. If $\beta_C < 1$, numerical simulations (5, 23, 27) generally agree that the noise is optimized for $\beta_L = 2LI_0/\Phi_0 \approx 1$, where L is the inductance of the SQUID. At elevated temperatures, shot noise is small compared to the classical Johnson noise, resulting in an estimated flux noise (5), $S_J \sim 16k_B TL^2/R$, valid for $\beta_L = 1$. At $T = 0$ K, shot noise and zero-point fluctuations contribute (24–27). When $\beta_L = 1$, their contributions are approximately $\hbar L$ and $\hbar L$, respectively.

R, L, and C can vary depending on the fabrication technology used and on the SQUID geometry. In SQUIDs on tips and nano-SQUIDs (see **Figure 1*a*,*b***), L is often limited by the kinetic inductance, which is determined by the penetration depth and superconducting film thickness. For Pb-based SQUIDs on tips, it is ~10 pH (11). In planar SQUIDs, there is a large, shielded loop, whose overall geometric inductance is ~80 pH (12). Both the kinetic and geometric inductance vary with the pickup loop size.

Figure 1*e* shows the magnetic field noise floor obtained for various sensors versus the loop size. The flux noise depends linearly on the loop radius, r, due to the loop inductance, but the magnetic noise has a $1/r^2$ dependence, so overall a smaller pickup loop results in a larger magnetic noise. For loops smaller than ~0.5 μm, SQUIDs on tips are favorable, because their kinetic inductance is smaller than the geometrical inductance of the entire planar-SQUID structure. For larger loops, the inductance of SQUIDs on tips is comparable with the planar SQUIDs. In this case, planar SQUIDs offer better noise performance, because the multilayer structure allows for optimizing the critical currents and junction capacitance.

The optimal magnetometer for a given application may not be the one with the lowest magnetic noise or the smallest spatial resolution. The choice depends on the magnetic field profile of the sample. The magnetic fields from various sources decay differently with the source-sensor distance. For example, the field from a point dipole decays as $1/r^3$, whereas the field from current in a wire decays as $1/r$. The minimal sensor-sample distance depends on the SQUID design. It is 100–500 nm for planar SQUIDs, and 50–100 nm for SQUIDs on tips (loop diameter 50–100 nm). For dipoles, the signal gain from closer proximity to the sample outweighs the sensitivity loss due to the smaller effective area of the SQUID, but not for the fields from the electric currents that extend farther in the lateral directions (**Figure 1*f*,*g***).

Modifying the basic SQUID design enables additional functionality. For example, a planar SQUID can be upgraded to a susceptometer by adding a coil concentric to the pickup loop and measuring the mutual inductance (12, 28). A SQUID on a tip can be used as a thermometer when its temperature-dependent critical current couples to the sample via exchange gas (29).

SUPERCONDUCTIVITY

Superconductors were among the first materials to be imaged with SQUIDs (30). Famously, scanning SQUIDs were used to study the order parameter symmetry in the cuprates, for example, by detecting half integer flux quantization in $YBa_2Cu_3O_{7-\delta}$ rings, directly confirming the *d*-wave order parameter for the first time (31). We refer the reader to Reference 2 for a comprehensive review of these discoveries, and to References 32–37 for more recent vortex-related works. Here, we focus on SQUID susceptometry, particularly in the context of possible unconventional superconductors.

In the past decade, two-dimensional (2D) superconductors have attracted considerable interest, as advances in fabrication techniques allowed the study of crystalline 2D superconductors, with thicknesses from a few nanometers (38) to a single atomic layer (39, 40). Superconductivity in these systems is inferred from the temperature dependence of their magnetoresistance and current-voltage characteristics, but the fundamental Meissner effect is evasive due to the large penetration lengths. One approach to directly measure the diamagnetic response is local mutual inductance measurements (**Figure 2*a***). In this technique, current is applied to a one-turn coil (field coil) concentric to the pickup loop, serving as a magnetic field source. The superconductor responds to the applied field by generating screening currents, whose magnetic signature is then detected by the SQUID's pickup loop. The combination of the local perturbation and proximity to the superconductor enables mapping variations in the superfluid density and detecting effective penetration depths (Pearl lengths) up to several millimeters (**Figure 2*b***; 41–43). The screening supercurrents, induced in the superconductor, mirror the current in the field coil. Close to the critical temperature (or at high enough fields) flux penetrates the superconductor, and the shielding currents, which flow in a closed loop, must maintain fluxoid quantization. This grants the SQUID susceptometer access to quantum phase information, in particular, the ability to track phase fluctuations near the transition (43, 44).

The sensitivity to large penetration depths and to both the amplitude and the phase of the order parameter allow investigating the fluctuations at the onset of superconductivity. In superconducting systems that go through a quantum phase transition, quantum fluctuations drive the transition. These fluctuations are well studied theoretically but much harder to detect directly. Kremen et al. (43) used a SQUID susceptometer to map fluctuations near criticality in NbTiN, which appeared as large fluctuating quantized reductions of the local superfluid density. These fluctuations were manifested as telegraph-like noise in the superfluid density when measured as a function of time (**Figure 2*c***) and as fluctuating puddles as a function of position. These puddles were larger than expected theoretically—tens of microns (rather than the size of the coherence length, tens of nanometers)—and the timescales (seconds) were longer than expected (45, 49). These findings highlight the role of spatial and temporal complexity of quantum fluctuations in the microscopic description of quantum transitions.

Heavy fermion superconductors are another class of materials raising puzzling questions. When magnetic exchange interactions compete with Kondo screening (50, 51), superconductivity may emerge, often alongside or competing with other orders or in proximity to a quantum phase transition (52, 53). Determining the phase diagram in these systems may help determine the origin of superconductivity, but it remains a challenging task for many materials.

When inhomogeneity is present, it is often difficult to determine its relevance to the overall picture. For example, a superconducting percolative path forming at a temperature above the average bulk T_c may produce discrepancies between T_c inferred from heat capacity and resistivity. Such superconducting paths may arise in disordered superconductors (54) or one-dimensional (1D) superconductors (55) but could also originate from other effects. For example, Bachmann et al. (56) mapped T_c variations in $CeIrIn_5$, finding that T_c is higher near the edges of the sample.

These spatial modulations arise from thermal expansion mismatch between samples and substrate and may explain why some sample geometries show higher resistive T_c (57).

Additionally, it is challenging to determine whether coexisting orders cooperate or compete. For example, superconducting ferromagnets may host a spontaneous vortex phase (58), where vortices form even after the sample is zero-field cooled. Conversely, superconductivity can alter the magnetic domain structure (59). There were several attempts to learn about such interplay from

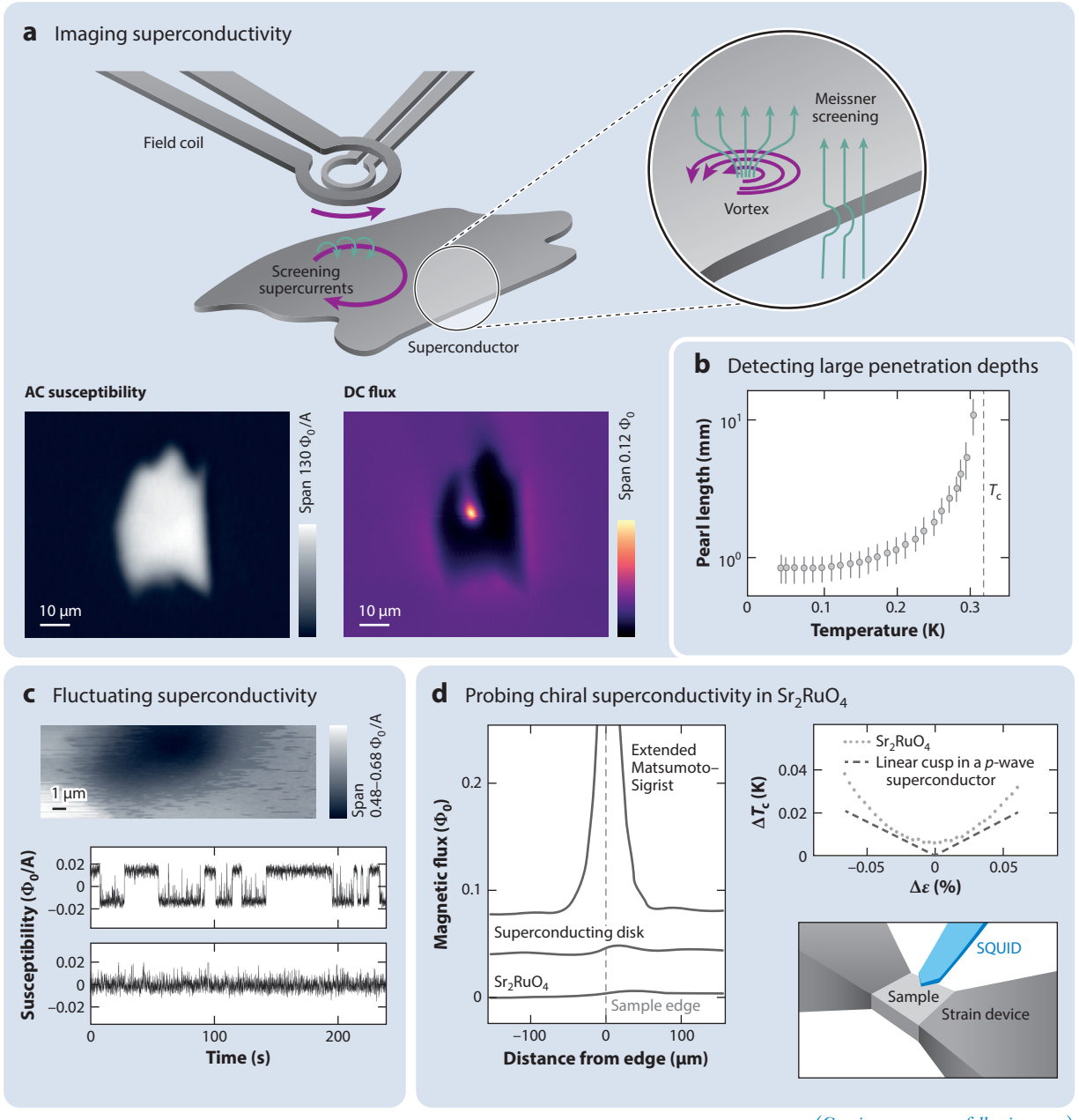

(*Caption appears on following page*)

Figure 2 (*Figure appears on preceding page*)

Scanning SQUID imaging of superconductors. (*a*, *top*) Local mutual inductance measurements applied to a superconductor. Current in a loop concentric to the SQUID's pickup coil generates magnetic fields at the sample. The superconductor then generates screening currents, which produce fields detectable by the SQUID. (*a*, *top*, *inset*) Other magnetic field profiles typical in superconductors: distorted field lines near the edge, due to the Meissner effect, and a vortex. (*a*, *bottom*) Simultaneous AC susceptibility (*left*) and DC flux (*right*) images of a superconducting flake showing Meissner screening and an isolated vortex. (*b*) Large Pearl lengths at the $LaAlO_3$–$SrTiO_3$ two-dimensional interface detected by local mutual inductance (46). (*c*) Spatial (*top*) and temporal (*bottom*) fluctuations in the local susceptibility of a NbTiN thin film close to a quantum critical point (43). (*d*) Efforts to detect chiral superconductivity in Sr_2RuO_4. (*d*, *left*) Magnetic field near the edge of the crystal, which is much smaller than the fields predicted from chiral edge currents (47). (*d*, *top right*) Locally measured changes in T_c owing to uniaxial strain, inconsistent with the linear dependence expected for a *p*-wave superconductor (48). (*d*, *bottom right*) Illustration of the experimental setup used to apply uniaxial strain simultaneous to scanning. Panel *b* adapted with permission from Reference 46. Panel *c* adapted with permission from Reference 43. Panel *d* (*left*) adapted with permission from Reference 47. Panel *d* (*right*) adapted with permission from Reference 48.

SSM experiments. Paulsen et al. (60) and Hykel et al. (61) imaged the magnetic landscape of superconducting ferromagnet UCoGe. Although indirectly observed via other methods (62), both studies did not directly resolve individual spontaneous vortices. One possible explanation for this is that the signal from spontaneous vortices is much smaller than the signal from the ferromagnetic domains. Another explanation is that the vortices are too dense to be spatially resolved by the sensors. Furthermore, in both studies, the ferromagnetic domain patterns did not change after zero-field-cooling the sample through the superconducting transition. Applying an external field within the superconducting state resulted in small changes to the ferromagnetic structure near the edge of the sample. This suggests that the change is due to Meissner currents rather than an interplay between the superconducting and magnetic orders. Similarly, in URu_2Si_2, inhomogeneous ferromagnetism appeared below 16.4 K and remained unchanged in the superconducting phase ($T_c = 1.5$ K; 63). The discrepancy between theory and observations suggests that a more detailed model is required. Particularly, existing theory does not capture the case in which ferromagnetic domains are similar in size to the penetration depth. This missing part is important, because vortices form near T_c, where the penetration depth is large. On the experimental side, better control over the ferromagnetism is required to clarify the picture.

Time-reversal symmetry breaking can also coexist with superconductivity through chiral superconductivity. In such superconductors, Cooper pairs have a nonzero total angular momentum (64), which is expected to result in topologically protected states at sample edges and chiral domain boundaries. Although multiple experimental tests exist (65), different experimental investigations often lead to conflicting results; Sr_2RuO_4 is perhaps the most studied example (66, 67). Extensive studies of this material resulted in contradictory conclusions, and the pairing symmetry is still debated (68). Spatially resolving edge mode signatures could provide additional information. Specifically, chiral edge states produce spontaneous currents, which generate magnetic fields. Several SQUID studies tried to directly detect these fields in Sr_2RuO_4 (47, 69) and URu_2Si_2 (70). The signals detected were much smaller than predicted by theory (**Figure 2*d***, *left*), placing strict limits on the magnitude of spontaneous currents, and on chiral domain size.

Recently, strain has emerged as a symmetry-sensitive probe of the superconducting order parameter (71–73). For example, for a $p_x \pm ip_y$ order parameter, uniaxial strain is predicted to lift the degeneracy of the p_x and p_y components, giving rise to a split superconducting transition, with overall T_c that depends linearly on strain (74). Watson et al. (48) imaged superconductivity in Sr_2RuO_4 under uniaxial stress and did not detect the linear strain dependence, which was in agreement with global susceptibility measurements (71), placing further limits on *p*-wave superconductivity (**Figure 2*d***, *right*). Ultrasound experiments (72, 73) confirmed a two-component order parameter but did not confirm or exclude chirality. Recent muon

spin relaxation experiments on strained samples are consistent with a chiral superconductor (75). Furthermore, the theoretical predictions for spontaneous magnetic fields in chiral superconductors have been revisited (76), indicating that the signal can be weak, depending on system-specific surface properties. A more detailed theory is therefore required to assist with further SQUID experiments aimed at exploring the magnetic behavior of chiral superconducting candidates.

MAGNETISM

Bulk ferromagnets often generate strong signals, making them accessible not only to SQUIDs but also to other magnetic imaging techniques like Hall probes or magneto-optics. The high sensitivity of SSM is required when magnetism coexists with other properties, as demonstrated in the section titled Superconductivity for ferromagnetic superconductors, and when the magnetic volume is small like in magnetic nanoparticles (77), 2D systems, and other dilute localized moments (41, 78–81).

1D systems like magnetic nanowires are predicted to have magnetic textures different than bulk ferromagnets (82), but directly confirming these predictions is challenging due to the small signals generated by individual nanowires. Nano-SQUIDs can be used in two ways: first, a nanowire can be placed on a stationary nano-SQUID loop (**Figure 3*a***; 83–85). This approach provides the best coupling between the nanowire and the SQUID but does not allow direct imaging. Alternatively, the magnetic signals can be imaged with a scanning SQUID. Although the nanowires are typically smaller than the SQUID loop, the magnetic fields they generate can be used to infer the underlying magnetic textures. Buchter et al. (86) and Nagel et al. (10) used this method to investigate the magnetization reversal of individual ferromagnetic Ni nanotubes. They observed abrupt changes to the magnetization, corresponding to multidomain states, but could not directly resolve the magnetic texture of each domain. In hybrid InAs–EuS–Al nanowires the magnetic field maps were consistent with single domains aligned along the nanowire, confirming that shape anisotropy controls the magnetization (87), which might help in the research endeavor of creating Majorana bound states.

When analyzing magnetic systems, the magnetic moment distribution, $\mathbf{M}(\mathbf{r})$, rather than the magnetic field, $\mathbf{B}(\mathbf{r})$, is often the quantity of interest. When magnetic moments are sparse, a point dipole model can be fitted to each localized signal, and the moment distribution can be extracted from the SSM images (**Figure 3*b***; 41, 78, 79, 93). However, for a general $\mathbf{M}(\mathbf{r})$, the reconstruction process from the $\mathbf{B}(\mathbf{r})$ data is nonunique (94). Finite spatial resolution and sensor-sample distance further limit the ability to resolve dense magnetic domains (**Figure 3*c***). For example, Wang et al. (89) reported magnetic domains in $LaMnO_3$–$SrTiO_3$ interfaces, above a critical $LaMnO_3$ thickness (**Figure 3*d***, *left*). These domains were associated with ferromagnetism, which was suggested to originate in electronic reconstruction at the interface. However, Anahory et al. (90) found that the magnetic domains are smaller than originally thought (**Figure 3*d***, *right*), and this led to an alternative interpretation, where metallic superparamagnetic islands form in an insulating antiferromagnetic matrix. A more detailed study of the temporal magnetic fluctuations is needed to resolve the exact microscopic mechanism of the magnetic ordering.

Superparamagnetism can also be investigated using time-dependent measurements. Lachman et al. (95, 96) found magnetic relaxation signatures of the quantum phase transition between two anomalous Hall effect plateaus in a Cr-doped $(Bi,Sb)_2Te_3$, implying that superparamagnetic fluctuations may be one of the limiting factors in realizing the quantum anomalous Hall effect at high temperatures. When fluctuating magnetism cannot be spatially resolved, it can still be detected by measuring the out-of-phase susceptibility. For example, in $EuCd_2P_2$ with interlayer antiferromagnetic and intralayer ferromagnetic orders, Wang et al. (97) used a scanning SQUID susceptometer to image fluctuating moments as the out-of-phase component of the local AC

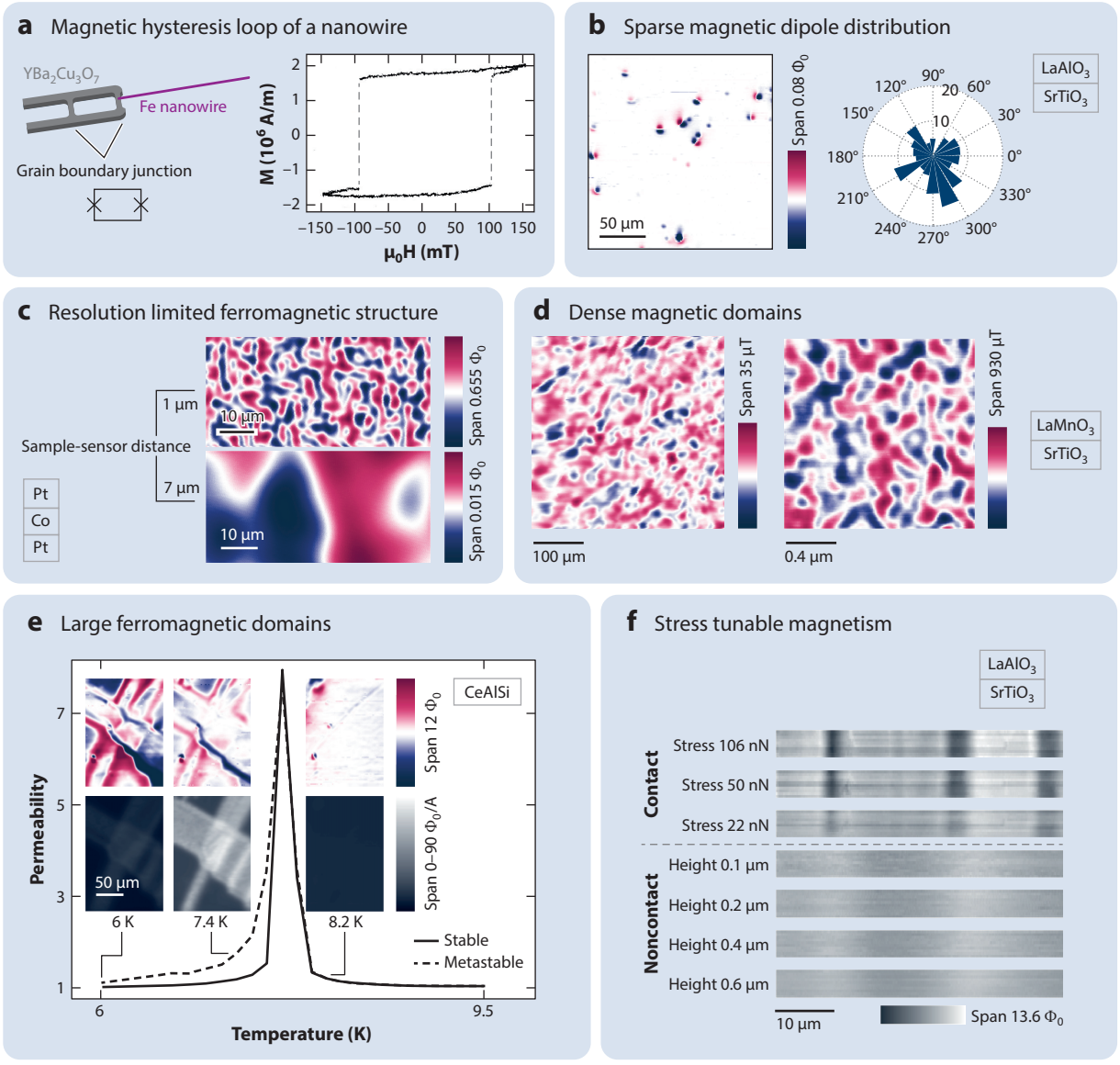

Figure 3

SSM in magnetic material systems. (*a*, *left*) A magnetic nanowire coupled to a nano-SQUID. (*a*, *right*) The small SQUID pickup loop and proximity to the wire allow high field measurements of the wire's hysteresis loop (88). (*b*) Sparse dipoles can be resolved and quantitatively analyzed (41, 78). (*c*) A complex magnetic landscape (*top*) is smeared (*bottom*) when the sensor is displaced from the sample. (*d*) Magnetic patterns in $LaMnO_3$ thin film imaged by sensors with different spatial resolutions. The similarity between the images suggests that in both cases individual domains cannot be resolved (89, 90). (*e*) Domain boundaries can be resolved when the domains are large. Simultaneous susceptibility measurements diverge near the magnetic transition and identify two distinct coexisting magnetic phases (91). (*f*) Stress-induced magnetism at an oxide interface. The tip of the sensor applies stress to the sample while simultaneously measuring the magnetic fields (92). Panel *a* adapted with permission from Reference 88. Panel *b* adapted with permission from References 41 and 78. Panel *d* adapted with permission from References 89 (*left*) and 90 (*right*). Graph in panel *e* adapted with permission from Reference 91. Panel *f* adapted with permission from Reference 92. Abbreviation: SSM, scanning SQUID microscopy.

magnetic susceptibility. These fluctuations acted as strong scatterers for conduction electrons, suggesting that the colossal magnetoresistance in $EuCd_2P_2$ arises from magnetic fluctuations rather than from heterovalent ion moments like in manganates.

Boundaries of extended objects, such as large magnetic domains, can be resolved by SSM. For instance, Xu et al. (91) discovered metastable domain-like regions in CeAlSi (**Figure 3*e***), a noncentrosymmetric Weyl semimetal (98). The metastable regions were identified as regions that can be annealed by field or temperature treatments. These regions formed boundaries around large in-plane stable ferromagnetic domains and shrunk upon annealing, down to narrow domain walls, while the stable ones expanded. The stable and metastable domains can be differentiated in susceptibility maps; they bifurcate at the ferromagnetic transition temperature identified by a divergent permeability (**Figure 3*e***), with higher out-of-phase values characterizing the metastable regions. These heterogenous magnetic textures are important to understand because interfaces between different (strained) magnetic states in a Weyl semimetal are predicted to host regions with emergent topological electrodynamics due to shifts of the Weyl cones (99). When combined with other methods, such as dynamic excitations, SSM could facilitate the discovery of these emergent topological effects.

In $SrTiO_3$, Christensen et al. (92) discovered a long-range stripe-like magnetic order that overlaps with the ferroelastic domain structure. They showed that the magnetism and susceptibility can be tuned by applying local external stress (**Figure 3*f***), clarifying magneto-transport measurements in $SrTiO_3$-based conducting interfaces, which suggested that itinerant electrons are coupled to magnetism of unknown nature. The magnetism may arise from multiferroicity at the domain walls, but the exact microscopic origin remains an open question. One possibility is that dynamic magnetism is induced by circular-like ion motion in the lattice (100, 101) or by domain wall motion (102).

DIRECT IMAGING OF TOPOLOGICAL EDGE MODES

The key signature of topologically nontrivial order is a metallic surface or edge state of a material that is otherwise insulating (103). The quantum Hall effect (QHE) and 2D topological insulators (TIs) are two prominent examples of topological order in two dimensions (104). Both TI and QHE systems can be identified through their unique transport signatures. Their metallic edges are protected from backscattering, so they support dissipationless current flow with quantized conductance (105–108). Nonetheless, in TIs, quantized conductance is only observed in small devices (107), implying that backscattering occurs. Direct visualization of current flow and dissipation can clarify the mechanisms behind dissipation in topologically protected channels.

Edge currents in a 2D TI were first directly imaged in 2013 (109). Nowack et al. imaged the magnetic fields generated by current flow in HgTe quantum wells. In these structures, electrostatic gating tunes the Fermi level from the valance band through the bulk gap. The SQUID images clearly identified edge and bulk flow, as they generate distinct magnetic field signals (**Figure 4*a***). If current flows both in the bulk and on the edges, the magnetic signature is a linear combination of the two extremes, weighed by the proportion of current in each channel. From such data, the conductivity of the edge modes relative to the bulk can be inferred. Spanton et al. (110) used this method to investigate the temperature dependence of edge conductivity in InAs–GaSb quantum wells. They found an anomalous temperature dependence: the relative resistance of the bulk increased with decreasing temperature, but the resistance of the edge modes did not depend on temperature. The high resistance of the edge modes ($\gg h/2e^2$) proves that scattering must occur, but the mechanism is not trivial. Elastic scattering, which has no temperature dependence, is forbidden at the helical edge modes, and inelastic scattering generically leads to power-law temperature dependence, which cannot be reconciled with experiments.

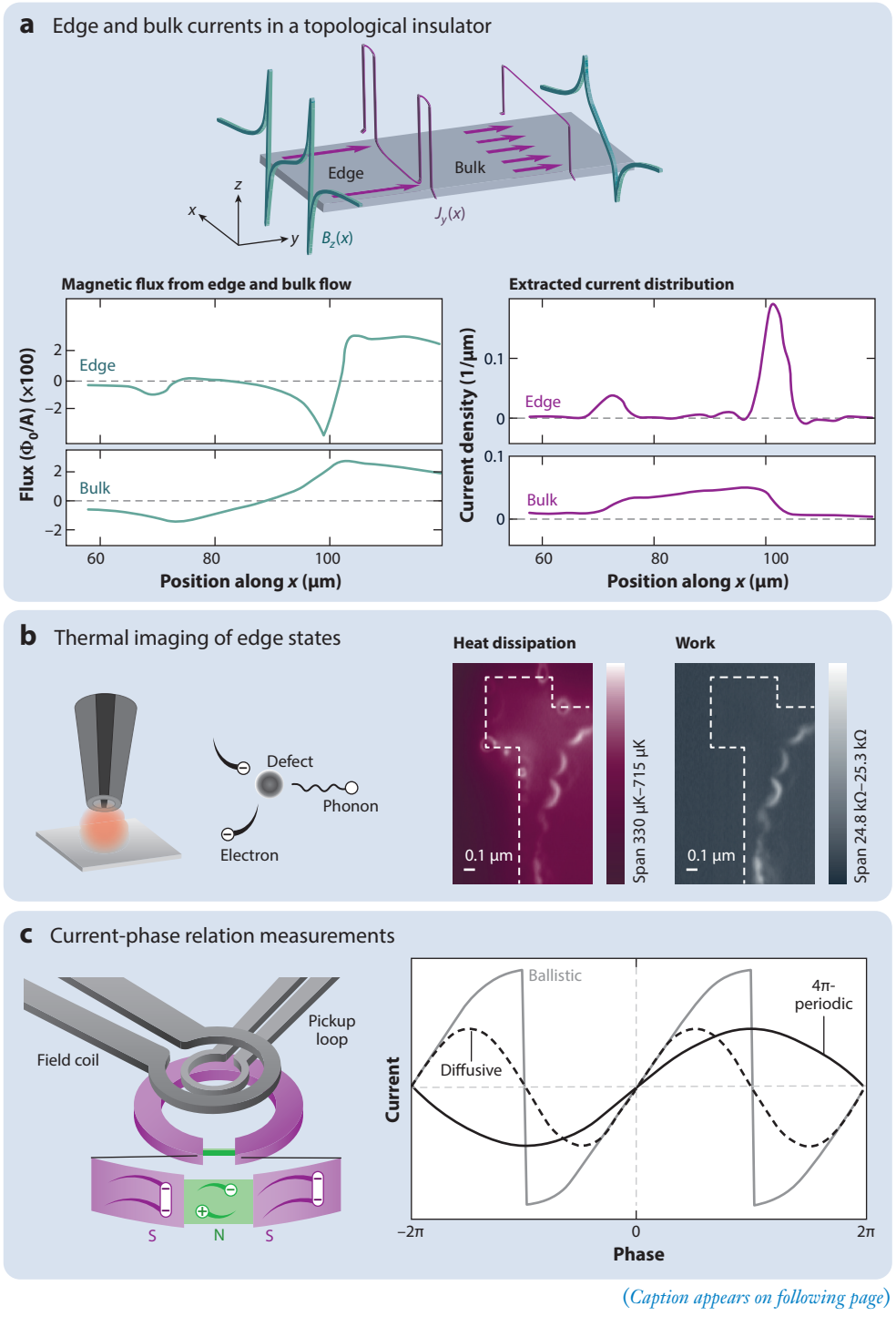

(*Caption appears on following page*)

Figure 4 (*Figure appears on preceding page*)

Studying topological states. (*a*, *top*) Current density (*purple*) and resulting magnetic field (*green*) profiles of edge and bulk currents in two dimensions. Edge currents generate sharp variations at the edges of the sample, whereas bulk flow results in smooth field variations to the magnetic field across the device. (*a*, *bottom*) Magnetic flux (*left*) and reconstructed current density (*right*) from a HgTe quantum well in its topological and trivial states. The transition between the two was tuned by a gate voltage (109). (*b*, *left*) Schematic of thermal imaging using a SQUID. Local heating in the sample couples to the sensor via exchange gas (*red sphere*), changing the critical current of the SQUID. (*b*, *middle*) In graphene, heat dissipation mostly occurs through scattering from defects (29, 111). (*b*, *right*) Heat dissipation and work maps for the quantum Hall state in graphene. The dashed line indicates the sample edge (112). Work maps are generated by using the SQUID as a local top gate. (*c*, *left*) CPR measurements with SSM. The field coil induces circulating currents in a superconducting ring, setting a phase difference across the Josephson junction. The circulating current is detected by the pickup loop as flux proportional to the Josephson current. (*c*, *right*) Three examples of theoretical CPR forms: a sinusoidal 2π-periodic form expected in a diffusive regime; a skewed relation expected in a ballistic point contact; a 4π-periodic form expected for Majorana modes in the junction. Panel *a* adapted with permission from Reference 109. Panel *b* (*right*) adapted with permission from Reference 111. Panel *b* (*left*) adapted with permission from Reference 112. Abbreviations: CPR, current–phase relation; N, normal; S, superconductor; SSM, scanning SQUID microscopy.

A direct path for investigating scattering in topological systems is through imaging heat dissipation. This approach was implemented by Marguerite et al. when investigating edge modes in the QHE phase in graphene (112). They simultaneously mapped heat dissipation and used the SQUID as a scanning gate, imaging local changes to the sample's resistance due to the gate voltage (**Figure 4*b***). Such changes in resistance correspond to work generated in the system. The heat dissipation and resistance maps differed, suggesting two coexisting mechanisms for heat dissipation at the chiral edge channels. Both mechanisms involve nonlocal processes, where work generates energy at one spatial point, but heat is dissipated at a different location. In the first mechanism, work is done where electrons tunnel between edge states, but heat is dissipated at atomic defects at the sample edge, through resonant electron–phonon coupling (111). This mechanism does not change the quantized conductance as it does not involve backward scattering. In the second mechanism, work is done through backscattering due to tunneling between topologically protected quantum Hall channels and edge-reconstructed, nonprotected edge modes. By directly imaging the edge currents, Uri et al. (113) confirmed that the topological and nontopological edge states are counter-propagating. These results suggest that the nontopological band-bending modes are important to consider when designing experiments such as those invoking proximity-induced superconductivity and nonlocal transport (114).

As more topological materials are discovered (115, 116), future research will be directed at understanding interacting topological systems, where questions about the interplay between electron interactions and topological protection await experimental answers (117). Like their nontopological counterparts, interacting topological materials could give rise to phenomena such as magnetism and superconductivity. The competition or coexistence of these phases make SSM a promising candidate for future discoveries.

CURRENT–PHASE RELATIONS IN JOSEPHSON JUNCTIONS

Tunneling experiments are a common approach to investigate the electronic properties of materials: The differential conductance of a tunnel junction probes the density of states in the junction material. A complementary approach is measuring the current–phase relation (CPR) of JJ devices. The CPR describes how the critical current, I_c, of a JJ depends on the phase drop, φ, across the junction. For a superconductor–trivial insulator–superconductor tunnel junction the CPR is $I_c = I_0 \sin(\phi)$, which is 2π-periodic (118, 119). Different tunneling barriers can lead to

more complex CPRs that may be represented as

$$I_c = \sum_{m,n} I_{m,n} \sin(\phi m/n + \Delta\phi_{m,n}),$$

where m and n are integers, m/n determines the fundamental periodicity (π, 2π, 4π, etc.), and $\Delta\phi_{m,n}$ are phase shifts in each component (120–122). In the case of 2π periodicity this equation simplifies to $I_c = \sum_m I_m \sin(m\phi + \Delta\phi_m)$. Each electronic energy mode in the junction contributes to the critical current measured as the CPR. Therefore, the periodicity and amplitude of the Josephson current are determined by the electronic structure of the junction. If the JJ is inserted into a superconducting ring, the CPR can be measured via the mutual inductance between the ring and a SQUID susceptometer (**Figure 4*c***). This contactless scanning approach is sometimes advantageous over electrical measurements, as it allows collecting statistics on many devices in a single cooldown and avoiding artifacts from transport leads and trapped vortices.

The earliest examples of measuring the CPR-driven properties are in cuprate tri-crystal rings, where SQUID measurements directly confirmed a π phase shift, due to the *d*-wave order parameter. In these experiments, the junctions were formed by interfacing three crystals (123). A π phase shift was also observed in superconductor–ferromagnet–superconductor junctions because Cooper pairs acquire a finite momentum when tunneling through the ferromagnetic layer (124). Bluhm et al. used a similar mutual inductance measurement method to observe persistent currents in single normal metal rings, confirming previous experiments on ensembles of rings (125). In superconducting rings, CPR-like measurements revealed unusual size-effect-driven fluctuation of the order parameter (126, 127).

The CPR can complement tunneling experiments by adding phase information and can be used for material characterization. For example, when the tunneling barrier is a TI, surface states are expected to be highly transmitting (128), giving rise to a skewed CPR (**Figure 4*c***). Sochnikov et al. found a trivial (sinusoidal) CPR in Al rings interrupted by TI Bi_2Se_3 (129), suggesting that the transport is dominated by the large trivial bulk conductivity in Bi_2Se_3 rather than the edge states. Conversely, a forward skewed CPR was found in strained HgTe [three-dimensional (3D) TI] junctions (119, 120) owing to its low bulk conductivity compared to the surface states (130).

Motivated by ideas for tunable superconducting devices and proposals for realization of Majorana modes, Spanton et al. studied Al rings with gate-tuned InAs nanowire junctions (121). In these devices, the amplitude and shape of the CPR varied between junctions. The small critical currents and skewed CPRs indicated few-mode junctions with high transmission. Gated devices showed extremely skewed CPRs with high critical currents, consistent with resonant tunneling through a single, highly transmitting mode. In a later study, Hart et al. (122) found effects of electron–electron interactions in JJs of InAs coated with epitaxial Al, where the junctions were controlled with three voltage gates, similar to a quantum dot. As a result of the interactions, the CPR exhibited a shoulder near $\pi+2\pi n$ phase.

Overall, these results bear potential for applications in highly tunable qubit-like devices. Particularly, SSM with higher bandwidths, in the megahertz–gigahertz regime, could use CPR measurements to access quasiparticle dynamics. Higher bandwidths can be helpful in direct characterization of Majorana modes (131), as they circumvent slower processes such as quasiparticle poisoning (132, 133).

LATTICE STRUCTURE AND ELECTRONIC PROPERTIES

Electrons reside in a host lattice, which determines the properties of the electrons it hosts. At the unit-cell level, composition and interatomic distances establish the band structure, from which

much of the electronic behavior stems. On a larger scale, it is structural defects, such as grain boundaries or strain profiles, which modify electronic properties. Directly imaging electronic properties on these scales eliminates the need for a priori determination of domain structure and design of experiment-specific samples. Tools like SSM are therefore ideal for uncovering relationships between electronic properties and mesoscopic structural features.

In this section, we demonstrate these capabilities by surveying recent work on $SrTiO_3$. At room temperature, $SrTiO_3$ is a cubic perovskite, but its low symmetry structure is tetragonal with a structural transition at 105 K. Stoichiometric $SrTiO_3$ is insulating, but doped $SrTiO_3$ is one of the most dilute superconductors (134). 2D conductivity and superconductivity at the $SrTiO_3$ surface can also be achieved, for example, by epitaxial growth of $LaAlO_3$ films (135). The transport properties of $SrTiO_3$-based 2D systems reveal a puzzling picture (136–138). On one hand, clean, high-mobility devices are routinely grown, and different groups report on qualitatively similar observations, including superconductivity, Shubnikov–de Haas (SdH) oscillations and gate tunable metal–insulator and superconductor–insulator transitions. On the other hand, there are inconsistencies, particularly at low temperatures. For example, carrier densities measured by Hall effect and SdH effect systematically disagree and carrier densities, mobilities and effective masses vary (138), even for samples grown in identical conditions. In 3D $SrTiO_3$, specific heat and resistivity measurements of the superconducting transition reveal different critical temperatures (139), indicating filamentary superconductivity. These results indicate that inhomogeneity is important for $SrTiO_3$ phenomenology, and its ubiquity suggests an intrinsic source.

SSM identified a candidate for such intrinsic inhomogeneity: structural domain boundaries. Imaging current flow in $LaAlO_3$–$SrTiO_3$ heterostructures, Kalisky et al. (140) observed long, narrow stripes of enhanced current flow embedded in a metallic background (**Figure 5*a***) and oriented along the crystallographic directions of $SrTiO_3$. New current flow patterns appeared after thermal cycles above the structural transition (105 K). Furthermore, due to the flexo-electric effect, exerting local stress on domain boundaries resulted in changes to the global conductivity of the 2D electron gas (2DEG) (**Figure 5*c***; 141). Both the current flow modulations and flexo-electric response decreased with increasing temperature, vanishing at ∼40 K. The temperature dependence coincides with the large changes to the dielectric constant of $SrTiO_3$ at low temperatures (142, 143). These results link the conductivity modulations at the 2DEG to the structural domain patterns.

The typical length of domain boundaries, tens of microns, is comparable with the size of mesoscopic devices fabricated with $SrTiO_3$-based heterostructures, suggesting domain structures may profoundly affect the transport properties. For example, in $LaAlO_3$–$SrTiO_3$ van der Pauw devices, Frenkel et al. identified correlations between resistance anisotropy and domain patterns (145; **Figure 5*b***). Furthermore, near the gate-tunable metal–insulator transition, current flow focused into narrow channels along the boundaries, resulting in a dimensional crossover from bulk 2D conduction to resolution-limited quasi 1D paths (144; **Figure 5*d***). Changes to domain configurations, particularly between different samples, can therefore strongly modify the details of the electronic transport.

It is natural to ask, How much of the $SrTiO_3$ phenomenology can be explained by domain patterns? Conductive tip atomic force microscopy can sketch conducting 1D nanowires on $LaAlO_3$–$SrTiO_3$, which may resemble the highly conducting narrow channels that naturally occur at the interface. In such nanowires, magnetoresistance oscillations (150) can be ascribed to a field-induced depopulation of the 1D subbands rather than 2D SdH oscillations. If domain boundaries share the properties of sketched 1D wave guides, their contribution to magnetotransport could account for the inconsistencies in carrier density measurements. In superconducting films grown on $SrTiO_3$, Noad et al. (146) and Wissberg & Kalisky (147) found correlations between the superfluid density and tetragonal domain patterns (**Figure 5*e***). In δ-doped $SrTiO_3$, domain

patterns resulted in T_c variations of ~10% (146), suggesting that the reported filamentary superconducting structure is related to domain patterns.

In the past decade, imaging efforts focused on understanding the extent to which domain patterns in $SrTiO_3$ may influence transport. However, the mechanism for these effects remains

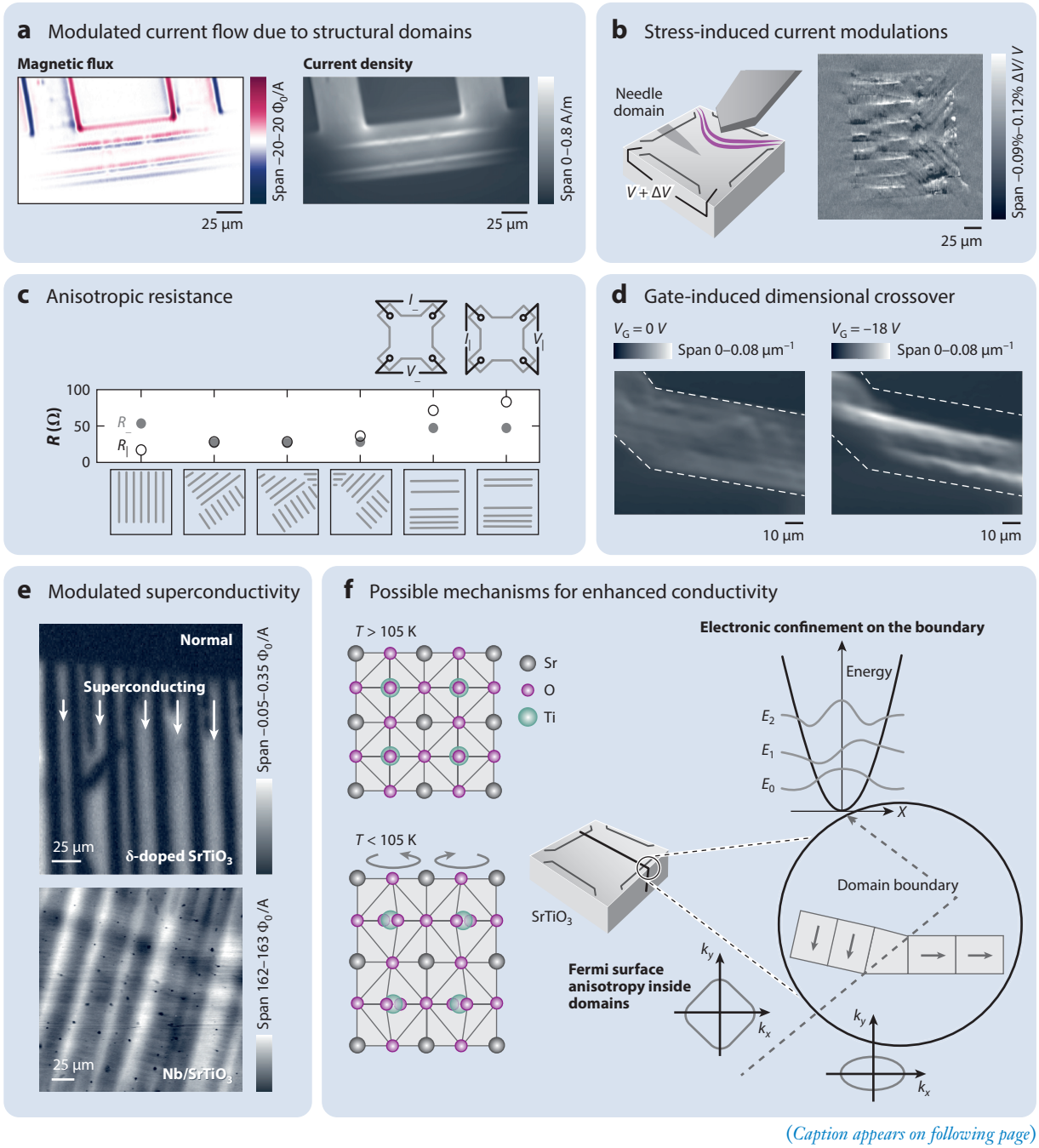

(Caption appears on following page)

Figure 5 (*Figure appears on preceding page*)

Interplay between structural domains and electronic properties in $SrTiO_3$. (*a*) Magnetic flux (*left*) and current density (*right*) in $LaAlO_3$–$SrTiO_3$, showing two stripes with enhanced conductivity along the [100] crystallographic direction, due to the $SrTiO_3$ domain structure (144). (*b*) Scanning stress combined with SQUID imaging, revealing a flexo-electric response at needle domain walls (141). (*c*, *top*) Transport anisotropy measured in a 200-μm $LaAlO_3$–$SrTiO_3$ square pattern following several thermal cycles above the structural transition. (*c*, *bottom*) The $SrTiO_3$ domain patterns after each cycle explain the change in anisotropy (145). (*d*) Current density maps of a $LaAlO_3$–$SrTiO_3$ device at two back-gate voltages, showing how, at low carrier densities, current flow is focused into narrow lines along domain patterns (144). (*e*) Local superfluid density affected by $SrTiO_3$ domain patterns in δ-doped $SrTiO_3$ (*top*) and a Nb thin film on $SrTiO_3$ substrate (*bottom*) (146, 147). (*f*, *left*) $SrTiO_3$ crystal structure in the cubic (*top*) and tetragonal (*bottom*) phases, demonstrating the elongation of the unit cell and the rotation of the oxygen octahedra. (*f*, *right*) Two possible mechanisms for conductivity modulations. Enhanced conductivity could be caused by electronic confinement at the domain boundaries (148), or by distortions of the Fermi surface at different domains, resulting in enhanced, anisotropic conductivity (149). Panels *a* and *d* adapted from Reference 144 (CC BY 4.0). Panel *b* adapted with permission from Reference 141. Panel *c* adapted with permission from Reference 145. Panel *e* (*top*) adapted with permission from Reference 146. Panel *e* (*bottom*) adapted from Reference 147 (CC BY 4.0).

elusive, and it is unclear whether electronic properties are modified by boundaries or by the domains themselves (**Figure 5*f***; 148–151). It is also unknown whether the mechanism is unique to $SrTiO_3$ or shared with other systems. On one hand, $SrTiO_3$ has a unique almost-ferroelectric state at low temperature (143), so it is possible that a ferroelectric state is induced near the interface, which may affect the electronic properties (152, 153). On the other hand, structural domains also affect properties of systems without a ferroelectric instability (154, 155). To answer these questions, it will be essential to gain control over domain formation in order to design samples for testing specific properties.

OUTLOOK

We demonstrated how SSM provides insights into electronic behavior in quantum materials. With more research groups turning to magnetic imaging, SQUIDs will continue to explore how electronic behavior is manifested on the mesoscale and reveal new electronic phenomena. There are several material systems of interest, accessible to the current generation of SQUID microscopes: topological Kondo insulators and semimetals, chiral superconductors, Moiré heterostructures, and more. These systems contain interesting interplays between magnetism and other electronic orders. SQUID experiments already provided information about twist-angle disorder (156) and orbital magnetism (157) in twisted bilayer graphene. For other applications, like troubleshooting quantum circuits, the magnetic field source might not be localized on a mesoscopic scale. Then, high field sensitivity is advantageous over spatial resolution, requiring SQUIDs with large (millimeter) pickup coils, which offer magnetic noise down to 1 $fT/(Hz)^{1/2}$ (15, 16) but have limited scanning capabilities.

Some systems of interest require a modified sensor or microscope design. For example, measurement in a high magnetic field is essential to access fractional quantum Hall states. High field operation can be achieved, for example, by using different superconducting materials. For example, a SQUID on a tip fabricated from $Mo_{66}Re_{34}$ can operate at fields up to 5 T (158), and $YBa_2Cu_3O_7$ nano-SQUIDs can operate at fields up to 7 T (9, 88). Another limitation is operating temperature: Elevated temperatures are required, for example, to access the strange metal phase in some high T_c superconductors. One solution is to fabricate SQUIDs from high-T_c superconductors. For example, Martínez-Pérez et al. (159) fabricated $YBa_2Cu_3O_7$-based SQUIDs that operated at temperatures up to 80 K. Another approach is to thermally decouple the sensor and the sample, thus avoiding increased thermal noise. This approach has enabled measurements with Nb SQUIDs, with sample temperatures up to 90 K (140, 160). In all cases, further work is required to optimize the noise performance in the extended operation conditions.

For other experiments, higher bandwidths are required. For example, magnetic excitations like magnons in ferromagnets (161–163) or spinons in spin liquids (164) occur at microwave frequencies. One direction is to use a SQUID as the field-sensitive inductive element of an LC resonator. Flux threading the SQUID changes its inductance, shifting the resonance frequency of the LC circuit (165–167). This scheme allows improved noise performance and a higher bandwidth, currently up to 200 MHz. Foroughi et al. (168) recently fabricated such scanning SQUIDs with 1-μm pickup loop and 80-nΦ_0/(Hz)$^{1/2}$ flux noise. A second approach is developing pump–probe capabilities. In this scheme, a hysteretic SQUID is driven into its resistive state with a current pulse, generated with a Josephson pulse generator (169). The SQUID bias is chosen so that it is sensitive to external flux only during the pulse, so measuring its resistance captures the magnetic flux through the loop during the pulse. This approach overcomes the frequency limitations of room temperature electronics and enables operating frequency up to the Josephson frequency, typically hundreds of gigahertz. Cui et al. (170) recently used this approach to achieve 40-ps time resolution (25 GHz).

To conclude, as materials research advances, and access to high-quality material systems increases, the importance of local magnetic microscopy studies is evident. SSM is unique in its ability to detect multiple types of electronic properties; it is a feature that becomes essential when dealing with quantum materials. With extended operating capabilities, next-generation SQUIDs will be able to handle an even larger class of materials, providing essential information for deep understanding of correlated electron systems.

DISCLOSURE STATEMENT

The authors are not aware of any affiliations, memberships, funding, or financial holdings that might be perceived as affecting the objectivity of this review.

ACKNOWLEDGMENTS

We thank J.R. Kirtley, K.A. Moler, E. Zeldov, D. Koelle, K. Hasselbach, X.R. Wang, and J. Franklin for valuable feedback, comments, and discussions, and H. Hilgenkamp, K. Nowack, Y. Anahory, H. Noad, and A. Aharon for providing data. E.P and B.K. were supported by the European Research Council Grant No. ERC-2019-COG-866236, the Israeli Science Foundation Grant No. ISF-1251/19, COST Action CA16218, and the QuantERA ERA-NET Cofund in Quantum Technologies, Project No. 731473. I.S. acknowledges partial support from the United States Department of Defense.

LITERATURE CITED

1. Hartmann U. 1999. *Annu. Rev. Mater. Sci.* 29(1):53–87
2. Kirtley JR. 2010. *Rep. Prog. Phys.* 73(12):126501
3. Casola F, van der Sar T, Yacoby A. 2018. *Nat. Rev. Mater.* 3(1):17088
4. Josephson BD. 1962. *Phys. Lett.* 1(7):251–53
5. Clarke J, Braginski AI, eds. 2004. *The SQUID Handbook Vol. I*. Berlin: Wiley-VCH
6. Lam SKH, Tilbrook DL. 2003. *Appl. Phys. Lett.* 82(7):1078–80
7. Cleuziou J-P, Wernsdorfer W, Bouchiat V, Ondarçuhu T, Monthioux M. 2006. *Nat. Nanotechnol.* 1(1):53–59
8. Troeman AGP, Derking H, Borger B, Pleikies J, Veldhuis D, Hilgenkamp H. 2007. *Nano Lett.* 7(7):2152–56
9. Schwarz T, Nagel J, Wölbing R, Kemmler M, Kleiner R, Koelle D. 2013. *ACS Nano*. 7(1):844–50
10. Nagel J, Buchter A, Xue F, Kieler OF, Weimann T, et al. 2013. *Phys. Rev. B.* 88(6):064425
11. Vasyukov D, Anahory Y, Embon L, Halbertal D, Cuppens J, et al. 2013. *Nat. Nanotechnol.* 8:639–44

12. Huber ME, Koshnick NC, Bluhm H, Archuleta LJ, Azua T, et al. 2008. *Rev. Sci. Instrum.* 79(5):053704
13. Koshnick NC, Huber ME, Bert JA, Hicks CW, Large J, et al. 2008. *Appl. Phys. Lett.* 93(24):243101
14. Kirtley JR, Paulius L, Rosenberg AJ, Palmstrom JC, Holland CM, et al. 2016. *Rev. Sci. Instrum.* 87(9):093702
15. Sochnikov I, Davino D, Kalisky B. 2020. *Phys. Rev. Appl.* 14(1):014020
16. Ruffieux S, Kalaboukhov A, Xie M, Chukharkin M, Pfeiffer C, et al. 2020. *Supercond. Sci. Technol.* 33(2):025007
17. Anahory Y, Naren HR, Lachman EO, Buhbut Sinai S, Uri A, et al. 2020. *Nanoscale* 12(5):3174–82
18. Ketchen MB, Kirtley JR. 1995. *IEEE Trans. Appl. Supercond.* 5(2):2133–36
19. van Schendel PJA, Hug HJ, Stiefel B, Martin S, Güntherodt H-J. 2000. *J. Appl. Phys.* 88(1):435–45
20. Kazakova O, Puttock R, Barton C, Corte-León H, Jaafar M, et al. 2019. *J. Appl. Phys.* 125(6):060901
21. Rondin L, Tetienne J-P, Hingant T, Roch J-F, Maletinsky P, Jacques V. 2014. *Rep. Prog. Phys.* 77(5):056503
22. Barry JF, Schloss JM, Bauch E, Turner MJ, Hart CA, et al. 2020. *Rev. Mod. Phys.* 92(1):015004
23. Tesche CD, Clarke J. 1977. *J. Low Temp. Phys.* 29(3–4):301–31
24. Koch RH, Van Harlingen DJ, Clarke J. 1980. *Phys. Rev. Lett.* 45(26):2132–35
25. Dahm AJ, Denenstein A, Langenberg DN, Parker WH, Rogovin D, Scalapino DJ. 1969. *Phys. Rev. Lett.* 22(26):1416–20
26. Ketchen MB, Clarke J, Goubau WM. 1978. *AIP Conf. Proc.* 44(1):22–27
27. Koch RH, Van Harlingen DJ, Clarke J. 1981. *Appl. Phys. Lett.* 38(5):380–82
28. Herrera C, Franklin J, Božović I, He X, Sochnikov I. 2021. *Phys. Rev. B.* 103(2):024528
29. Halbertal D, Cuppens J, Ben Shalom M, Embon L, Shadmi N, et al. 2016. *Nature* 539(7629):407–10
30. Kirtley JR, Wikswo JP. 1999. *Annu. Rev. Mater. Sci.* 29(1):117–48
31. Tsuei CC, Kirtley JR, Chi CC, Yu-Jahnes LS, Gupta A, et al. 1994. *Phys. Rev. Lett.* 73(4):593–96
32. Kalisky B, Kirtley JR, Analytis JG, Chu J-H, Fisher IR, Moler KA. 2011. *Phys. Rev. B.* 83(6):064511
33. Kremen A, Wissberg S, Haham N, Persky E, Frenkel Y, Kalisky B. 2016. *Nano Lett.* 16(3):1626–30
34. Embon L, Anahory Y, Jelić ŽL, Lachman EO, Myasoedov Y, et al. 2017. *Nat. Commun.* 8(1):85
35. Zhang IP, Palmstrom JC, Noad H, Bishop-Van Horn L, Iguchi Y, et al. 2019. *Phys. Rev. B.* 100(2):024514
36. Llorens JB, Embon L, Correa A, González JD, Herrera E, et al. 2020. *Phys. Rev. Res.* 2(1):013329
37. Ceccarelli L, Vasyukov D, Wyss M, Romagnoli G, Rossi N, et al. 2019. *Phys. Rev. B.* 100(10):104504
38. Saito Y, Nojima T, Iwasa Y. 2016. *Nat. Rev. Mater.* 2(1):16094
39. Benyamini A, Telford EJ, Kennes DM, Wang D, Williams A, et al. 2019. *Nat. Phys.* 15(9):947–53
40. Cao Y, Fatemi V, Fang S, Watanabe K, Taniguchi T, et al. 2018. *Nature* 556(7699):43–50
41. Bert JA, Kalisky B, Bell C, Kim M, Hikita Y, et al. 2011. *Nat. Phys.* 7(10):767–71
42. Bert JA, Nowack KC, Kalisky B, Noad H, Kirtley JR, et al. 2012. *Phys. Rev. B.* 86(6):060503
43. Kremen A, Khan H, Loh YL, Baturina TI, Trivedi N, et al. 2018. *Nat. Phys.* 14(12):1205–10
44. Wissberg S, Frydman A, Kalisky B. 2018. *Appl. Phys. Lett.* 112(26):262602
45. Ghosal A, Randeria M, Trivedi N. 1998. *Phys. Rev. Lett.* 81(18):3940–43
46. Bert JA. 2012. *Superconductivty in reduced dimensions*. PhD Thesis, Stanford University, Stanford, California
47. Kirtley JR, Kallin C, Hicks CW, Kim E-A, Liu Y, et al. 2007. *Phys. Rev. B.* 76(1):14526
48. Watson CA, Gibbs AS, Mackenzie AP, Hicks CW, Moler KA. 2018. *Phys. Rev. B.* 98(9):094521
49. Sacépé B, Chapelier C, Baturina TI, Vinokur VM, Baklanov MR, Sanquer M. 2008. *Phys. Rev. Lett.* 101(15):157006
50. Stewart GR. 1984. *Rev. Mod. Phys.* 56(4):755–87
51. Wirth S, Steglich F. 2016. *Nat. Rev. Mater.* 1(10):16051
52. Gegenwart P, Si Q, Steglich F. 2008. *Nat. Phys.* 4(3):186–97
53. Si Q, Steglich F. 2010. *Science* 329(5996):1161–66
54. Pelc D, Anderson Z, Yu B, Leighton C, Greven M. 2019. *Nat. Commun.* 10(1):2729
55. Nagata S, Ebisu S, Aochi T, Kinoshita Y, Chikazawa S, Yamaya K. 1991. *J. Phys. Chem. Solids.* 52(6):761–67
56. Bachmann MD, Ferguson GM, Theuss F, Meng T, Putzke C, et al. 2019. *Science* 366(6462):221–26

57. Shang T, Baumbach RE, Gofryk K, Ronning F, Weng ZF, et al. 2014. *Phys. Rev. B.* 89(4):041101
58. Ng TK, Varma CM. 1997. *Phys. Rev. Lett.* 78(2):330–33
59. Fauré M, Buzdin AI. 2005. *Phys. Rev. Lett.* 94(18):187202
60. Paulsen C, Hykel DJ, Hasselbach K, Aoki D. 2012. *Phys. Rev. Lett.* 109(23):237001
61. Hykel DJ, Paulsen C, Aoki D, Kirtley JR, Hasselbach K. 2014. *Phys. Rev. B.* 90(18):184501
62. Ohta T, Hattori T, Ishida K, Nakai Y, Osaki E, et al. 2010. *J. Phys. Soc. Jpn.* 79(2):023707
63. Iguchi Y, Zhang IP, Bauer ED, Ronning F, Kirtley JR, Moler KA. 2021. *Phys. Rev. B.* 103(22):L220503
64. Kallin C, Berlinsky J. 2016. *Rep. Prog. Phys.* 79(5):054502
65. Sigrist M, Ueda K. 1991. *Rev. Mod. Phys.* 63(2):239–311
66. Mackenzie AP, Maeno Y. 2003. *Rev. Mod. Phys.* 75(2):657–712
67. Mackenzie AP, Scaffidi T, Hicks CW, Maeno Y. 2017. *npj Quantum Mater.* 2(1):40
68. Kivelson SA, Yuan AC, Ramshaw B, Thomale R. 2020. *npj Quantum Mater.* 5(1):43
69. Hicks CW, Kirtley JR, Lippman TM, Koshnick NC, Huber ME, et al. 2010. *Phys. Rev. B.* 81(21):214501
70. Iguchi Y, Zhang IP, Bauer ED, Ronning F, Kirtley JR, Moler KA. 2021. *Phys. Rev. B* 103:L220503
71. Hicks CW, Brodsky DO, Yelland EA, Gibbs AS, Bruin JAN, et al. 2014. *Science* 344(6181):283–85
72. Benhabib S, Lupien C, Paul I, Berges L, Dion M, et al. 2021. *Nat. Phys.* 17(2):194–98
73. Ghosh S, Shekhter A, Jerzembeck F, Kikugawa N, Sokolov DA, et al. 2021. *Nat. Phys.* 17(2):199–204
74. Sigrist M, Joynt R, Rice TM. 1987. *Phys. Rev. B.* 36(10):5186–98
75. Grinenko V, Ghosh S, Sarkar R, Orain J-C, Nikitin A, et al. 2021. *Nat. Phys.* 17(6):748–54
76. Etter SB, Bouhon A, Sigrist M. 2018. *Phys. Rev. B.* 97(6):064510
77. Wernsdorfer W. 2009. *Supercond. Sci. Technol.* 22(6):064013
78. Kalisky B, Bert JA, Klopfer BB, Bell C, Sato HK, et al. 2012. *Nat. Commun.* 3(1):922
79. Persky E, Kalisky B. 2018. *Adv. Mater.* 30(41):1706653
80. Harada A, Taniyama T, Takeuchi Y, Sato T, Kyômen T, Itoh M. 2007. *Phys. Rev. B.* 75(18):184426
81. Kirtley JR, Kalisky B, Bert JA, Bell C, Kim M, et al. 2012. *Phys. Rev. B.* 85(22):224518
82. Staňo M, Fruchart O. 2018. In *Handbook of Magnetic Materials*, Vol. 27, ed. E Brück, pp. 155–267. Oxford, UK: Elsevier
83. Wernsdorfer W, Hasselbach K, Benoit A, Cernicchiaro G, Mailly D, et al. 1995. *J. Magn. Magn. Mater.* 151(1):38–44
84. Wernsdorfer W, Doudin B, Mailly D, Hasselbach K, Benoit A, et al. 1996. *Phys. Rev. Lett.* 77(9):1873–76
85. Martínez-Pérez MJ, Koelle D. 2017. *Phys. Sci. Rev.* 2(8):20175001
86. Buchter A, Nagel J, Rüffer D, Xue F, Weber DP, et al. 2013. *Phys. Rev. Lett.* 111(6):67202
87. Liu Y, Vaitiekėnas S, Martí-Sánchez S, Koch C, Hart S, et al. 2020. *Nano Lett.* 20(1):456–62
88. Schwarz T, Wölbing R, Reiche CF, Müller B, Martínez-Pérez MJ, et al. 2015. *Phys. Rev. Appl.* 3(4):044011
89. Wang XR, Li CJ, Lu WM, Paudel TR, Leusink DP, et al. 2015. *Science* 349(6249):716–19
90. Anahory Y, Embon L, Li CJ, Banerjee S, Meltzer A, et al. 2016. *Nat. Commun.* 7(1):12566
91. Xu B, Franklin J, Jayakody A, Yang H-Y, Tafti F, Sochnikov I. 2021. *Adv. Quantum Technol.* 4(3):2000101
92. Christensen DV, Frenkel Y, Chen YZ, Xie YW, Chen ZY, et al. 2019. *Nat. Phys.* 15(3):269–74
93. Wittlich P, Boschker H, Asaba T, Li L, Noad HML, et al. 2019. *Phys. Rev. Mater.* 3(10):104418
94. Clarke J, Braginski AI, eds. 2006. *The SQUID Handbook Vol. II*. Berlin: Wiley-VCH
95. Lachman EO, Young AF, Richardella A, Cuppens J, Naren HR, et al. 2015. *Sci. Adv.* 1(10):e1500740
96. Lachman EO, Mogi M, Sarkar J, Uri A, Bagani K, et al. 2017. *npj Quantum Mater.* 2(1):70
97. Wang Z-C, Rogers JD, Yao X, Nichols R, Atay K, et al. 2021. *Adv. Mater.* 33(10):2005755
98. Yang H-Y, Singh B, Gaudet J, Lu B, Huang C-Y, et al. 2021. *Phys. Rev. B.* 103(11):115143
99. Ilan R, Grushin AG, Pikulin DI. 2020. *Nat. Rev. Phys.* 2(1):29–41
100. Juraschek DM, Fechner M, Balatsky AV, Spaldin NA. 2017. *Phys. Rev. Mater.* 1(1):014401
101. Dunnett K, Zhu J-X, Spaldin NA, Juričić V, Balatsky AV. 2019. *Phys. Rev. Lett.* 122(5):057208
102. Juraschek DM, Meier QN, Trassin M, Trolier-McKinstry SE, Degen CL, Spaldin NA. 2019. *Phys. Rev. Lett.* 123(12):127601
103. Moore JE. 2010. *Nature* 464(7286):194–98
104. Hasan MZ, Kane CL. 2010. *Rev. Mod. Phys.* 82(4):3045–67
105. Klitzing KV, Dorda G, Pepper M. 1980. *Phys. Rev. Lett.* 45(6):494–97

106. Thouless DJ, Kohmoto M, Nightingale MP, den Nijs M. 1982. *Phys. Rev. Lett.* 49(6):405–8
107. Konig M, Wiedmann S, Brune C, Roth A, Buhmann H, et al. 2007. *Science* 318(5851):766–70
108. Kane CL, Mele EJ. 2005. *Phys. Rev. Lett.* 95(22):226801
109. Nowack KC, Spanton EM, Baenninger M, König M, Kirtley JR, et al. 2013. *Nat. Mater.* 12(9):787–91
110. Spanton EM, Nowack KC, Du L, Sullivan G, Du R-R, Moler KA. 2014. *Phys. Rev. Lett.* 113(2):026804
111. Halbertal D, Ben Shalom M, Uri A, Bagani K, Meltzer AY, et al. 2017. *Science* 358(6368):1303–6
112. Marguerite A, Birkbeck J, Aharon-Steinberg A, Halbertal D, Bagani K, et al. 2019. *Nature* 575(7784):628–33
113. Uri A, Kim Y, Bagani K, Lewandowski CK, Grover S, et al. 2020. *Nat. Phys.* 16(2):164–70
114. Aharon-Steinberg A, Marguerite A, Perello DJ, Bagani K, Holder T, et al. 2021. *Nature* 593(7860):528–34
115. Vergniory MG, Elcoro L, Felser C, Regnault N, Bernevig BA, Wang Z. 2019. *Nature* 566(7745):480–85
116. Tang F, Po HC, Vishwanath A, Wan X. 2019. *Nature* 566(7745):486–89
117. Rachel S. 2018. *Rep. Prog. Phys.* 81(11):116501
118. Golubov AA, Kupriyanov MY, Il'ichev E. 2004. *Rev. Mod. Phys.* 76(2):411–69
119. Beenakker CWJ, van Houten H. 1992. In *Nanostructures and Mesoscopic Systems*, ed. WP Kirk, MA Reed, pp. 481–97. Boston: Elsevier
120. Sochnikov I, Maier L, Watson CA, Kirtley JR, Gould C, et al. 2015. *Phys. Rev. Lett.* 114(6):066801
121. Spanton EM, Deng M, Vaitiekėnas S, Krogstrup P, Nygård J, et al. 2017. *Nat. Phys.* 13(12):1177–81
122. Hart S, Cui Z, Ménard G, Deng M, Antipov AE, et al. 2019. *Phys. Rev. B.* 100(6):064523
123. Kirtley JR, Tsuei CC, Sun JZ, Chi CC, Yu-Jahnes LS, et al. 1995. *Nature* 373(6511):225–28
124. Gingrich EC, Niedzielski BM, Glick JA, Wang Y, Miller DL, et al. 2016. *Nat. Phys.* 12(6):564–67
125. Bluhm H, Koshnick NC, Bert JA, Huber ME, Moler KA. 2009. *Phys. Rev. Lett.* 102(13):136802
126. Koshnick NC, Bluhm H, Huber ME, Moler KA. 2007. *Science* 318(5855):1440–43
127. Bert JA, Koshnick NC, Bluhm H, Moler KA. 2011. *Phys. Rev. B.* 84(13):134523
128. Tkachov G, Hankiewicz EM. 2013. *Phys. Rev. B.* 88(7):075401
129. Sochnikov I, Bestwick AJ, Williams JR, Lippman TM, Fisher IR, et al. 2013. *Nano Lett.* 13(7):3086–92
130. Hancock JN, van Mechelen JLM, Kuzmenko AB, van der Marel D, Brüne C, et al. 2011. *Phys. Rev. Lett.* 107(13):136803
131. Sun L, DiCarlo L, Reed MD, Catelani G, Bishop LS, et al. 2012. *Phys. Rev. Lett.* 108(23):230509
132. Serniak K, Hays M, de Lange G, Diamond S, Shankar S, et al. 2018. *Phys. Rev. Lett.* 121(15):157701
133. Karzig T, Cole WS, Pikulin DI. 2021. *Phys. Rev. Lett.* 126(5):057702
134. Collignon C, Lin X, Rischau CW, Fauqué B, Behnia K. 2019. *Annu. Rev. Condens. Matter Phys.* 10:25–44
135. Ohtomo A, Hwang HY. 2004. *Nature* 427(6973):423–26
136. Hwang HY, Iwasa Y, Kawasaki M, Keimer B, Nagaosa N, Tokura Y. 2012. *Nat. Mater.* 11(2):103–13
137. Sulpizio JA, Ilani S, Irvin P, Levy J. 2014. *Annu. Rev. Mater. Res.* 44(1):117–49
138. Pai Y-Y, Tylan-Tyler A, Irvin P, Levy J. 2018. *Reports Prog. Phys.* 81(3):036503
139. Lin X, Gourgout A, Bridoux G, Jomard F, Pourret A, et al. 2014. *Phys. Rev. B.* 90(14):140508
140. Kalisky B, Spanton EM, Noad H, Kirtley JR, Nowack KC, et al. 2013. *Nat. Mater.* 12(12):1091–95
141. Frenkel Y, Haham N, Shperber Y, Bell C, Xie Y, et al. 2017. *Nat. Mater.* 16(12):1203–8
142. Sakudo T, Unoki H. 1971. *Phys. Rev. Lett.* 26(14):851–53
143. Müller KA, Burkard H. 1979. *Phys. Rev. B.* 19(7):3593–602
144. Persky E, Vardi N, Monteiro AMRVL, van Thiel TC, Yoon H, et al. 2021. *Nat. Commun.* 12(1):3311
145. Frenkel Y, Haham N, Shperber Y, Bell C, Xie Y, et al. 2016. *ACS Appl. Mater. Interfaces.* 8(19):12514–19
146. Noad H, Spanton EM, Nowack KC, Inoue H, Kim M, et al. 2016. *Phys. Rev. B.* 94(17):174516
147. Wissberg S, Kalisky B. 2017. *Phys. Rev. B.* 95(14):144510
148. Pai Y-Y, Lee H, Lee J-W, Annadi A, Cheng G, et al. 2018. *Phys. Rev. Lett.* 120(14):147001
149. Tao Q, Loret B, Xu B, Yang X, Rischau CW, et al. 2016. *Phys. Rev. B.* 94(3):035111
150. Cheng G, Annadi A, Lu S, Lee H, Lee J-W, et al. 2018. *Phys. Rev. Lett.* 120(7):076801
151. Ma HJH, Scharinger S, Zeng SW, Kohlberger D, Lange M, et al. 2016. *Phys. Rev. Lett.* 116(25):257601
152. Rischau CW, Lin X, Grams CP, Finck D, Harms S, et al. 2017. *Nat. Phys.* 13(7):643–48
153. Tuvia G, Frenkel Y, Rout PK, Silber I, Kalisky B, Dagan Y. 2020. *Adv. Mater.* 32(29):2000216

154. Kalisky B, Kirtley JR, Analytis JG, Chu J-H, Vailionis A, et al. 2010. *Phys. Rev. B.* 81(18):184513
155. Davis SI, Ullah RR, Adamo C, Watson CA, Kirtley JR, et al. 2018. *Phys. Rev. B.* 98(1):014506
156. Uri A, Grover S, Cao Y, Crosse JA, Bagani K, et al. 2020. *Nature* 581(7806):47–52
157. Tschirhart CL, Serlin M, Polshyn H, Shragai A, Xia Z, et al. 2021. *Science* 372(6548):1323–27
158. Bagani K, Sarkar J, Uri A, Rappaport ML, Huber ME, et al. 2019. *Phys. Rev. Appl.* 12(4):044062
159. Martínez-Pérez MJ, Müller B, Schwebius D, Korinski D, Kleiner R, et al. 2016. *Supercond. Sci. Technol.* 30(2):024003
160. Bishop-Van Horn L, Cui Z, Kirtley JR, Moler KA. 2019. *Rev. Sci. Instrum.* 90(6):063705
161. Chumak AV, Vasyuchka VI, Serga AA, Hillebrands B. 2015. *Nat. Phys.* 11(6):453–61
162. Tabuchi Y, Ishino S, Noguchi A, Ishikawa T, Yamazaki R, et al. 2016. *C. R. Phys.* 17(7):729–39
163. Wei DS, van der Sar T, Lee SH, Watanabe K, Taniguchi T, et al. 2018. *Science* 362(6411):229–33
164. Balents L. 2010. *Nature* 464(7286):199–208
165. Hatridge M, Vijay R, Slichter DH, Clarke J, Siddiqi I. 2011. *Phys. Rev. B.* 83(13):134501
166. Levenson-Falk EM, Vijay R, Antler N, Siddiqi I. 2013. *Supercond. Sci. Technol.* 26(5):055015
167. Levenson-Falk EM, Antler N, Siddiqi I. 2016. *Supercond. Sci. Technol.* 29(11):113003
168. Foroughi F, Mol J-M, Müller T, Kirtley JR, Moler KA, Bluhm H. 2018. *Appl. Phys. Lett.* 112(25):252601
169. Faris SM. 1980. *Appl. Phys. Lett.* 36(12):1005–7
170. Cui Z, Kirtley JR, Wang Y, Kratz PA, Rosenberg AJ, et al. 2017. *Rev. Sci. Instrum.* 88(8):083703